Dipolar dynamos in stratified systems

R. Raynaud,[1,2]★ L. Petitdemange[1,2] and E. Dormy[1,3]

[1]*MAG (ENS/IPGP), LRA, Département de Physique, École normale supérieure, 24 rue Lhomond, F-75252 Paris Cedex 5, France*
[2]*LERMA, Observatoire de Paris, PSL Research University, CNRS, UMR 8112, F-75014 Paris, France*
[3]*IPGP, CNRS UMR 7154, F-75005 Paris, France*

ABSTRACT

Observations of low-mass stars reveal a variety of magnetic field topologies ranging from large-scale, axial dipoles to more complex magnetic fields. At the same time, three-dimensional spherical simulations of convectively driven dynamos reproduce a similar diversity, which is commonly obtained either with Boussinesq models or with more realistic models based on the anelastic approximation, which take into account the variation of the density with depth throughout the convection zone. Nevertheless, a conclusion from different anelastic studies is that dipolar solutions seem more difficult to obtain as soon as substantial stratifications are considered. In this paper, we aim at clarifying this point by investigating in more detail the influence of the density stratification on dipolar dynamos. To that end, we rely on a systematic parameter study that allows us to clearly follow the evolution of the stability domain of the dipolar branch as the density stratification is increased. The impact of the density stratification both on the dynamo onset and the dipole collapse is discussed and compared to previous Boussinesq results. Furthermore, our study indicates that the loss of the dipolar branch does not ensue from a specific modification of the dynamo mechanisms related to the background stratification, but could instead result from a bias as our observations naturally favour a certain domain in the parameter space characterized by moderate values of the Ekman number, owing to current computational limitations. Moreover, we also show that the critical magnetic Reynolds number of the dipolar branch is scarcely modified by the increase of the density stratification, which provides an important insight into the global understanding of the impact of the density stratification on the stability domain of the dipolar dynamo branch.

Key words: convection – dynamo – MHD – stars: magnetic field.

1 INTRODUCTION

Observations of low-mass stars reveal very different magnetic field topologies, ranging from small-scale fields to large-scale dipolar fields, and the last advances in spectropolarimetry should enable one to improve the understanding of the magnetic fields of solar-type stars (Donati & Landstreet 2009; Morin et al. 2010). Among the three suggestions advanced by Larmor to explain the generation of such magnetic fields (Larmor 1919), it is now the consensus that their decay is prevented by the action of self-excited dynamos induced by the turbulent motions that occur in stellar interiors. More often, these motions are assumed to be driven by convection, owing to the temperature difference between the inner core and the cooler surface. In dynamo theory, this partial transfer of the kinetic energy of a conducting fluid into magnetic energy is an instability process:

above a certain threshold, electrical currents start to be amplified by the fluid flow, so that a magnetic field can be sustained against the resistive decay due to ohmic dissipation.

After Glatzmaier & Roberts (1995), numerical modelling of self-consistent dynamos underwent considerable development (in contrast with the small number of successful experimental studies). However, despite the continuous increase of computer power, direct numerical simulations still face the difficulty to resolve a vast range of spatial and temporal scales when attempting to simulate a three-dimensional turbulent flow on a magnetic diffusion time-scale. As a simplification, one usually resorts to some convective approximations, and most of the early studies were relying on the Boussinesq approximation, which performs well as long as variations in pressure hardly affect the density of the fluid. However, this assumption is not valid to describe convection in large stratified systems such as stars or gas giants, in which the density typically varies over many scaleheights between the top and bottom of the convection zone. This limitation of the Boussinesq approximation

★ E-mail: raphael.raynaud@ens.fr

is basically what motivated the use of the anelastic approximation, originally developed to study atmospheric convection (Ogura & Phillips 1962; Gough 1969), to model convection in the Earth core and stellar interiors. Indeed, if we assume that the overall system remains close to an adiabatically stratified reference state at marginal stability so that convective motions can be treated as small perturbations (which in turns implies that typical velocities remain small compare to the speed of sound), then the anelastic approximation allows us to take some stratification into account while filtering out sound waves for faster numerical integration. This approximation can be found in the literature under slightly different formulations (Gilman & Glatzmaier 1981; Braginsky & Roberts 1995; Lantz & Fan 1999; Anufriev, Jones & Soward 2005; Berkoff, Kersale & Tobias 2010; Jones et al. 2011; Alboussière & Ricard 2013), which are in part compared in Brown, Vasil & Zweibel (2012).

Just as in Boussinesq models (Christensen & Aubert 2006; Schrinner, Petitdemange & Dormy 2012; Yadav et al. 2013), magnetic fields obtained in anelastic simulations (Gastine, Duarte & Wicht 2012; Duarte, Gastine & Wicht 2013; Schrinner et al. 2014) fall into two categories: dipolar dynamos, dominated by a large-scale axial dipole component, and multipolar dynamos, characterized by a more complex field topology with higher spatial and temporal variability. However, these studies identified several differences specific to anelastic dynamos. For instance, dipolar solutions seem more difficult to obtain as the density stratification is increased (Gastine et al. 2012; Jones 2014). We found in Schrinner et al. (2014) that for a given N_ϱ, E and Pr, there seems to exist a critical magnetic $\mathrm{Pm_c}$ below which the dipolar solution is not stable, and the higher the density stratification, the higher this critical magnetic Prandtl number. Furthermore, multipolar dynamos with a magnetic field configuration dominated by an equatorial dipole seem more easily realized with anelastic models than with Boussinesq models. However, we show in Raynaud, Petitdemange & Dormy (2014) that this characteristic also stands for weakly stratified models, since it is actually related to the use of different mass distributions. Indeed, the gravity profile may strongly influence the localisation of the convective cells, depending on whether one considers a homogeneous ($g \propto r$) or a central mass ($g \propto 1/r^2$) distribution: as opposed to the former, the latter results in the concentration of the convective cells close to the inner sphere, which favours the emergence of a less diffusive large-scale $m = 1$ mode at the outer surface of the model.

Our last study of weakly stratified models with a central mass distribution naturally constitutes an appropriate reference basis from which a detailed understanding of the role of the density stratification in anelastic dynamo models can be achieved. In this paper, we will primarily focus on dipolar dynamos. We aim at clarifying apparent contradictions between previous anelastic studies by investigating in more detail the evolution of the stability domain of the dipolar branch when increasing the density stratification. To that end, we rely on a systematic parameter study consisting of 119 three-dimensional, self-consistent dynamo models obtained by direct numerical simulations. As opposed to previous studies that were focusing on Jupiter's magnetic field (Duarte et al. 2013; Gastine et al. 2014; Jones 2014), we do not consider here more realistic models to reproduce a particular observation, but instead try to understand systematic and general tendencies in anelastic models, as a function of the physical control parameters. The anelastic equations are recalled in Section 2 and we present our results in Section 3. The complete list of numerical simulations performed for this study is given in Table A1 (see Appendix A).

2 EQUATIONS AND METHODS

Following Jones et al. (2011), we rely on the LBR formulation of the anelastic approximation (Lantz & Fan 1999; Braginsky & Roberts 1995). Actually, both the model and the numerical methods used here are the same as in Schrinner et al. (2014) and Raynaud et al. (2014) but we briefly recall them for completeness. We consider a spherical shell of width d and aspect ratio χ, rotating about the z-axis at angular velocity $\mathbf{\Omega}$ and filled with a perfect, electrically conducting gas with kinematic viscosity ν, thermal diffusivity κ, specific heat c_p and magnetic diffusivity η (all assumed to be constant). Convection is driven by an imposed entropy difference Δs between the inner and the outer boundaries, and the gravity is given by $\mathbf{g} = -GM\hat{\mathbf{r}}/r^2$, where G is the gravitational constant and M the central mass.

The reference state is given by the polytropic equilibrium solution of the anelastic system

$$\overline{P} = P_c\, w^{n+1}, \quad \overline{\varrho} = \varrho_c\, w^n, \quad \overline{T} = T_c\, w, \quad w = c_0 + \frac{c_1 d}{r}, \quad (1)$$

$$c_0 = \frac{2w_0 - \chi - 1}{1 - \chi}, \quad c_1 = \frac{(1 + \chi)(1 - w_o)}{(1 - \chi)^2}, \quad (2)$$

with

$$w_0 = \frac{\chi + 1}{\chi \exp(N_\varrho/n) + 1}, \quad w_i = \frac{1 + \chi - w_o}{\chi}. \quad (3)$$

In the above expressions, n is the polytropic index and $N_\varrho = \ln(\varrho_i/\varrho_o)$ the number of density scaleheights. The values P_c, ϱ_c and T_c are the reference-state density, pressure and temperature mid-way between the inner and outer boundaries, and serve as units for these variables.

Length is scaled by the shell width d, time by the magnetic diffusion time d^2/η and entropy by the imposed entropy difference Δs. The magnetic field is measured in units of $\sqrt{\Omega \varrho_c \mu \eta}$, where μ is the magnetic permeability. Then, the equations governing the system are

$$\frac{\partial \mathbf{v}}{\partial t} + (\mathbf{v} \cdot \nabla)\,\mathbf{v} = \mathrm{Pm}\left[-\frac{1}{E}\nabla\frac{P'}{w^n} + \frac{\mathrm{Pm}}{\mathrm{Pr}}\mathrm{Ra}\frac{s}{r^2}\hat{\mathbf{r}} - \frac{2}{E}\hat{\mathbf{z}} \times \mathbf{v} \right.$$
$$\left. + \mathbf{F}_\nu + \frac{1}{E\,w^n}(\nabla \times \mathbf{B}) \times \mathbf{B} \right], \quad (4)$$

$$\frac{\partial \mathbf{B}}{\partial t} = \nabla \times (\mathbf{v} \times \mathbf{B}) + \nabla^2 \mathbf{B}, \quad (5)$$

$$\frac{\partial s}{\partial t} + \mathbf{v} \cdot \nabla s = w^{-n-1}\frac{\mathrm{Pm}}{\mathrm{Pr}}\nabla \cdot \left(w^{n+1}\nabla s\right)$$
$$+ \frac{\mathrm{Di}}{w}\left[E^{-1}w^{-n}(\nabla \times \mathbf{B})^2 + Q_\nu \right], \quad (6)$$

$$\nabla \cdot \left(w^n \mathbf{v}\right) = 0, \quad (7)$$

$$\nabla \cdot \mathbf{B} = 0. \quad (8)$$

The viscous force $\mathbf{F}_\nu$ in equation (4) is given by $\mathbf{F}_\nu = w^{-n}\nabla \mathbf{S}$, where $\mathbf{S}$ is the rate of strain tensor

$$S_{ij} = 2w^n\left(e_{ij} - \frac{1}{3}\delta_{ij}\nabla \cdot \mathbf{v}\right), \quad e_{ij} = \frac{1}{2}\left(\frac{\partial v_i}{\partial x_j} + \frac{\partial v_j}{\partial x_i}\right). \quad (9)$$

Moreover, the expressions of the dissipation parameter Di and the viscous heating Q_ν in equation (6) are

$$\text{Di} = \frac{c_1 \text{Pr}}{\text{PmRa}}, \qquad (10)$$

and

$$Q_\nu = 2\left[e_{ij}e_{ij} - \frac{1}{3}(\nabla \cdot \boldsymbol{v})^2\right]. \qquad (11)$$

We impose stress-free boundary conditions for the velocity field at both the inner and the outer spheres, the magnetic field matches a potential field inside and outside the fluid shell, and the entropy is fixed at the inner and outer boundaries. Besides, both weak and strong field initial conditions have been tested for all models, since the system may exhibit hysteretic transitions between dynamo branches when stress-free boundary conditions are used.

The system of equations (4)–(8) involves seven control parameters, namely the Rayleigh number $\text{Ra} = GMd\Delta s/(\nu\kappa c_p)$, the Ekman number $E = \nu/(\Omega d^2)$, the Prandtl number $\text{Pr} = \nu/\kappa$ and the magnetic Prandtl number $\text{Pm} = \nu/\eta$, together with the aspect ratio χ, the polytropic index n and the number of density scaleheights N_ϱ that define the reference state. We choose $E = 10^{-4}$, $\text{Pr} = 1$ and $n = 2$. Different from Gastine et al. (2012), we also kept the central gravity profile and the aspect ratio $\chi = 0.35$ fixed for all simulations, but varied the magnetic Prandtl number, which turns out to be a key point to understand the partial divergence of our conclusions.

The equations are integrated in average for one magnetic diffusion time with the anelastic version of PARODY (Dormy, Cardin & Jault 1998; Schrinner et al. 2014).[1] The vector fields are transformed into scalars using the poloidal–toroidal decomposition. The equations are then discretized in the radial direction with a finite-difference scheme; on each concentric sphere, variables are expanded using a spherical harmonic basis. The coefficients of the expansion are identified with their degree ℓ and order m. Typical resolutions are 288 points in the radial direction (up to 320 points). The spectral decomposition is truncated at a hundred modes (up to $\ell_{\max} \sim m_{\max} \leq 128$), in order to observe for both spectra a decrease of more than two orders of magnitude over the range of l and m. The highest resolutions are required for the models with the highest density stratification ($N_\varrho = 3$).

The amplitudes of the velocity and the magnetic fields are measured in terms of the Rossby number $\text{Ro} = \sqrt{2E_k}E/\text{Pm}$ and Lorentz number $\text{Lo} = \sqrt{2E_m}E/\text{Pm}$, where E_k and E_m are the energy densities integrated over the fluid shell,

$$E_k = \frac{1}{2V}\int_V w^n \boldsymbol{v}^2 \, \mathrm{d}v \quad \text{and} \quad E_m = \frac{1}{2V}\frac{\text{Pm}}{E}\int_V \boldsymbol{B}^2 \, \mathrm{d}v. \qquad (12)$$

Likewise, the measure of the mean zonal flow is given by the zonal Rossby number Ro_z based on the averaged toroidal axisymmetric kinetic energy.

We also define a local Rossby number $\text{Ro}_\ell = \text{Ro}_c\, \ell_c/\pi$ based on the mean harmonic degree ℓ_c of the velocity component $\boldsymbol{v}_c$ from which the mean zonal flow has been subtracted (Schrinner et al. 2012, 2014),

$$\ell_c = \sum_\ell \ell \frac{\langle w^n (\boldsymbol{v}_c)_\ell \cdot (\boldsymbol{v}_c)_\ell \rangle}{\langle w^n \boldsymbol{v}_c \cdot \boldsymbol{v}_c \rangle}, \qquad (13)$$

where the brackets denote an average over time and radii. The contribution of the mean zonal flow is removed for calculating Ro_c.

[1] The integration times range from 0.63 to 5.2 magnetic diffusion times (for the models 101m and 004m, respectively).

Furthermore, as the stratification is increased, it turns out that it is useful to examine the variations with depth of the local Rossby number, defined in such a way that $\text{Ro}_\ell = \int_{r_i}^{r_o} \text{Ro}_\ell(r) r^2 \, \mathrm{d}r$. We found that it is more suitable to slightly adapt our initial definition and investigate the radial dependence of $\text{Ro}_\ell^\star(r)$, which differs from $\text{Ro}_\ell(r)$ in so far as the velocity is not weighted by the reference density profile w^n. We also checked that, in our range of N_ϱ, both estimates of a characteristic velocity do not make a qualitative difference on the volume-averaged quantities. For instance, the difference between the values of the magnetic Reynolds number $\text{Rm} = \text{RoPm}/E$ is about 1 per cent at $N_\varrho = 0.5$. Of course, it increases with N_ϱ: energy-based estimates lead to lower values about 7 and 10 per cent for $N_\varrho = 2.0$ and 2.5, respectively. However, this does not change our conclusions, and that is why we do not adapt our definition for volume-averaged quantities.

3 RESULTS

3.1 Bistability

Fig. 1 shows the distribution of dipolar and multipolar dynamos in the parameter space $(\text{Ra}/\text{Ra}_c, \text{Pm})$ (left-hand panels), together with the corresponding dipolarities (right-hand panels), for increasing density stratifications from top to bottom. One can see that several examples of bistable pairs are displayed. Bistability is commonly known for Boussinesq and anelastic models, and is related to the use of stress-free boundary conditions that allows for the growth of stronger zonal winds (Sasaki et al. 2011; Gastine et al. 2012; Schrinner et al. 2012). For $N_\varrho = 0.5$, the regime diagram in Fig. 1(a) does not qualitatively differ from what we can observe in the Boussinesq regime. As we found in Raynaud et al. (2014), the multipolar branch undergoes a supercritical bifurcation as Ra is increased, whereas the dipolar one still loses its stability in favour of the multipolar branch at low Rayleigh and magnetic Prandtl numbers. When increasing the density contrast N_ϱ to 1.5, one can note in Fig. 1(c) that the overlap between the two branches shrinks. At $N_\varrho = 2$, we do not observe a bistable case. More generally, for all models of our sample with a density stratification $N_\varrho \geq 2$, the saturated field of the dynamo is not anymore sensitive to the amplitude of the initial magnetic field. To understand this evolution from Boussinesq models to anelastic models with moderate stratification ($N_\varrho \leq 1.5$), it is worth stressing that the transition process from the multipolar to the dipolar branch triggered by the increase of Pm still applies to our sample of models (see Schrinner et al. 2012). Fig. 2(a) illustrates on a few cases the progressive merging of the multipolar branch which is indeed lost when its zonal Rossby number becomes comparable to the zonal Rossby number of the dipolar branch. For a given Rayleigh number, the fact that the mean zonal flow of the multipolar branch decreases with Pm (and eventually becomes too small to prevent the growth of the axial dipole) is actually the limiting factor of the upper extent of the multipolar branch in the left-hand panels of Fig. 1. This also emphasizes the essential role played by differential rotation in the dynamo mechanism of the multipolar branch, often accounted for in terms of Ω-effect.

Interestingly, the zonal Rossby number for multipolar dynamos substantially decreases between $N_\varrho = 0.5$ and 1.5 (see the blue and red squares in Fig. 2a), while it remains of the same order for dipolar dynamos. Hence, the available range of Pm for the multipolar solution is reduced, which therefore explains the relative shrinking of the bistable region when comparing Figs 1(a) and (c). The simplest argument to understand this downtrend is given by the comparison of the x-axis in Fig. 1, which reveals that the
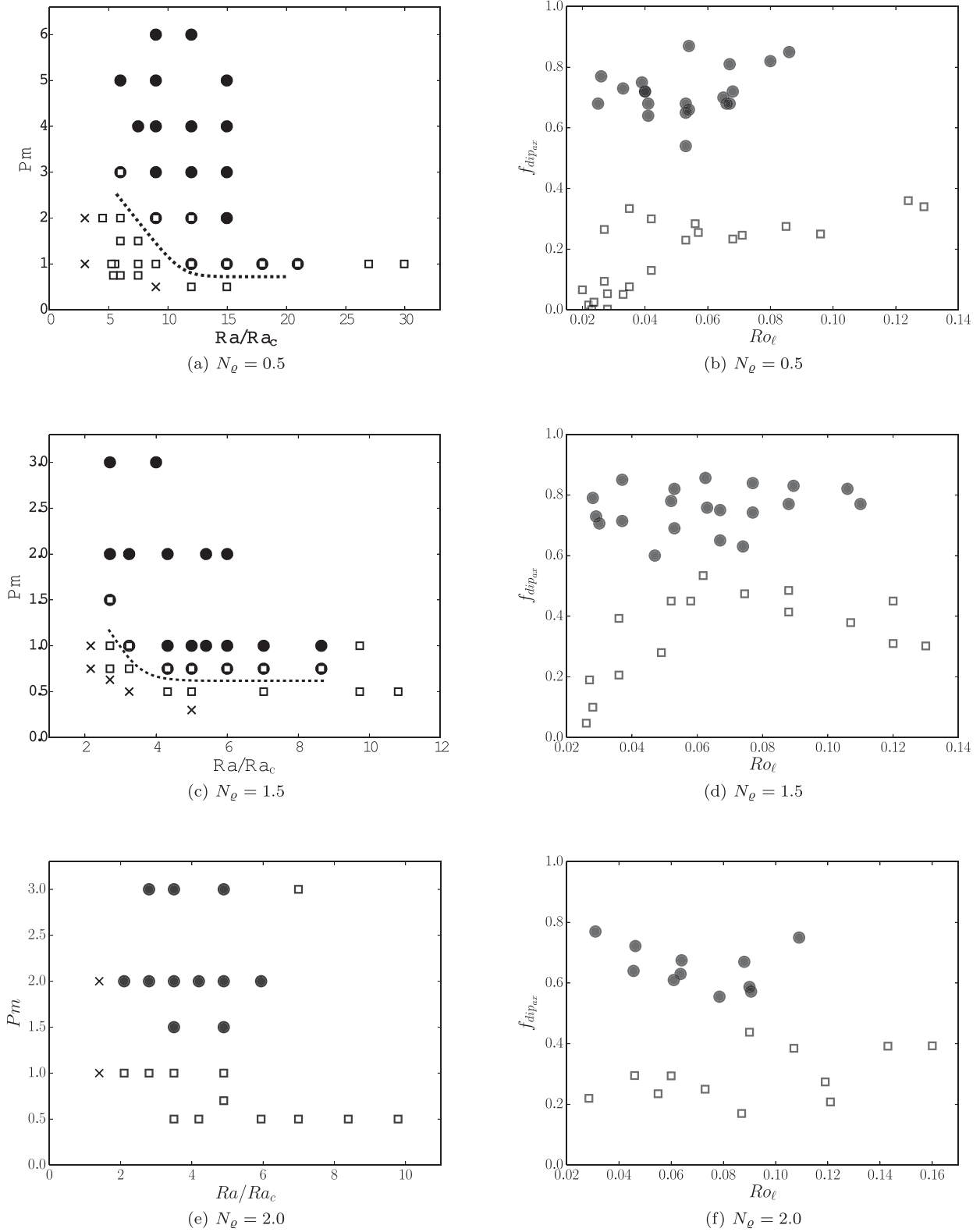
Figure 1. Left: dipolar (black circles) and multipolar (white squares) dynamos as a function of Ra/Ra$_c$ and Pm, for $N_\varrho = 0.5$ (a), $N_\varrho = 1.5$ (c) and $N_\varrho = 2.0$ (e). A cross indicates the absence of a self-sustained dynamo. Right: the relative axial dipole field strength $f_{\mathrm{dip_{ax}}}$ versus the local Rossby number for $N_\varrho = 0.5$ (b), $N_\varrho = 1.5$ (d) and $N_\varrho = 2.0$ (f).
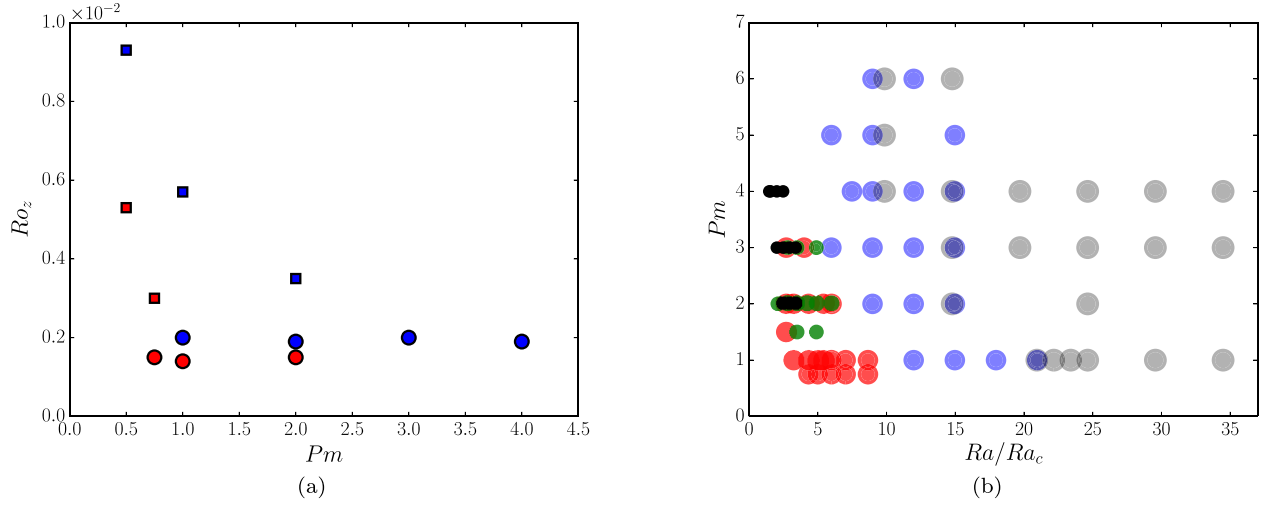
Figure 2. (a) Evolution of the zonal Rossby number as a function of Pm for a dynamo model with Ra $= 4 \times 10^6$, at $N_\varrho = 0.5$ (blue) and $N_\varrho = 1.5$ (red). Circles (squares) stand for dipolar (multipolar) dynamos. (b) Dipolar dynamos in the parameter space (Ra/Ra$_c$, Pm), for increasing density stratifications: $N_\varrho = 0.1$ (grey), $N_\varrho = 0.5$ (blue) $N_\varrho = 1.5$ (red), $N_\varrho = 2.0$ (green) and $N_\varrho = 2.5$ (black).
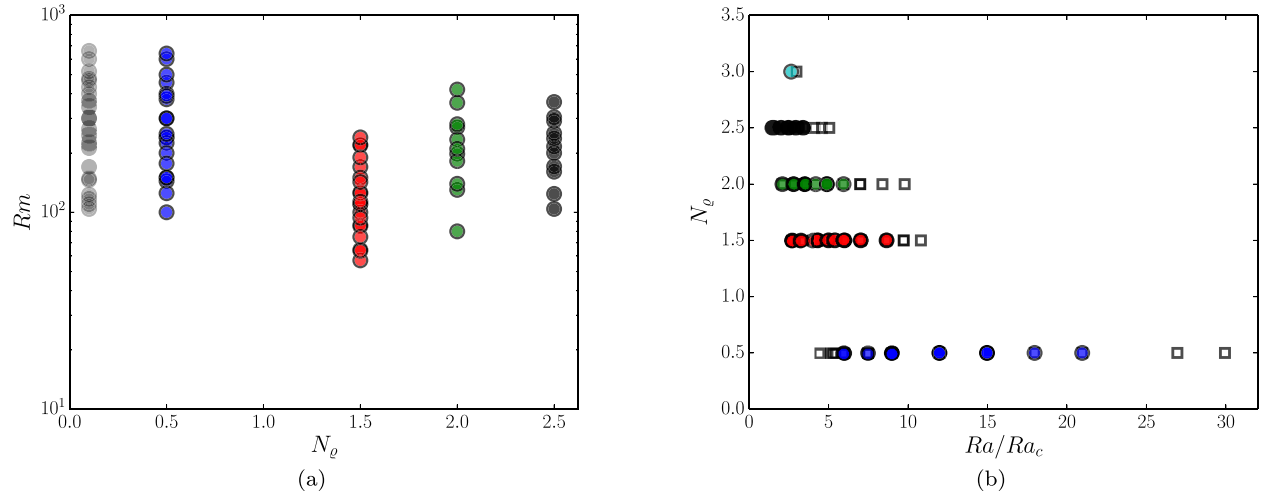
Figure 3. (a) Magnetic Reynolds number as a function of N_ϱ for dipolar dynamos. (b) Our sample of dipolar (circles) and multipolar (squares) dynamos in the parameter space (Ra/Ra$_c$, N_ϱ).

dynamo onset moves closer to the onset of convection when the density stratification is increased, as mentioned by Gastine et al. (2012). Indeed, despite changing the value of N_ϱ, we found that the Rayleigh numbers we had to consider always stay of the order of 10^6. At the same time, the critical Rayleigh number for the linear onset of convection monotonically increases with N_ϱ. From table B.1 in Schrinner et al. (2014), we have in our case the following values of 3.34×10^5, 9.25×10^5 and finally 1.43×10^6 for the sequence of density stratifications $N_\varrho = 0.5$, 1.5 and 2.0, respectively.

3.2 Dipole onset

The density stratification strongly impacts on the stability domain of the dipolar branch, as we clearly see in Fig. 2(b). In this figure, we included data from Raynaud et al. (2014) in order to better highlight the differences with Boussinesq simulations. For moderate values of N_ϱ at a fixed Pm, the critical value of Ra/Ra$_c$ at which it is possible to sustain a dipolar dynamo rapidly falls off (up to a factor of 4 if we

consider the line Pm $= 1$). However, this tendency hardly persists once we reach Ra/Ra$_c \sim 5$ for $N_\varrho = 1.5$, and the further increase of N_ϱ mainly affects the critical magnetic Prandtl number Pm$_c$ below which it is not possible to sustain a dipolar dynamo. In our sample of models, the increase of Pm$_c$ becomes effective for $N_\varrho \geq 2$, but we already reported it as a general tendency in Schrinner et al. (2014). Fig. 1(c) enables us to conclude that $0.5 < \text{Pm}_c \leq 0.75$ for $N_\varrho = 1.5$, whereas from Fig. 1(e), it is clear that Pm$_c > 1$ for $N_\varrho = 2$.

The fact that dipolar dynamos are found closer to the convection threshold as N_ϱ increases can be more or less readily understood if one notices that, despite the increase of the density stratification, the critical magnetic Reynolds number Rm$_c$ of the dipolar branch does not significantly vary, but stays in first approximation of the order of 10^2, as shown in Fig. 3(a). Then, if we take this as a necessary condition to obtain a dipolar solution, and given the fact that for a constant value of Ra/Ra$_c$ the flow amplitude increases with N_ϱ (Gastine et al. 2012), it explains why the dipolar branch can be found closer to the onset of convection when the stratification increases.

However, we will see in the next subsection that, as N_ϱ is further increased, not only does the dipolar branch occur closer to the onset of convection, but also higher magnetic Prandtl numbers have to be considered to maintain a sufficiently high Rm while preventing the collapse of the dipole.

3.3 Dipole collapse

Another striking feature that arises when investigating the stability domain of the dipolar branch is that the range of Rayleigh numbers over which it extends becomes smaller and smaller as N_ϱ is increased. This is clearly visible in Fig. 3(b) that shows for different N_ϱ the transition from the dipolar to the multipolar branch resulting from the increase of Ra. In other words, at this moderate value of the Ekman number, dipolar dynamos are confined in a narrower and narrower window of Rayleigh numbers, which explains why dipolar solutions may seem more difficult to obtain at higher N_ϱ, despite comparable critical magnetic Reynolds numbers. As for the modification of the dynamo onset, this can be related to the fact that for a given value of Ra/Ra$_c$, the Rossby number Ro increases with N_ϱ.[2] The transition from a dipolar to a multipolar solution triggered by an increase of Ra is related to the fact that inertia becomes significant in the force balance. We know from Christensen & Aubert (2006) that this transition can be measured by a local Rossby number Ro$_\ell$ based on a characteristic length-scale of the flow. We find that the collapse of the dipole still occurs for Ro$_\ell \sim 0.1$ when $N_\varrho \leq 2$, which is consistent with the results in Gastine et al. (2012). This is illustrated by Figs 1(b), (d) and (f) which show the relative axial dipole field strength $f_{\mathrm{dip}_{ax}}$ computed at the outer sphere, as a function of Ro$_\ell$. In Fig. 1(b), the very low values of $f_{\mathrm{dip}_{ax}}$ at low Ro$_\ell$ are characteristics of multipolar dynamos dominated by an equatorial dipole component. We showed in Raynaud et al. (2014) that this magnetic configuration arises close to the dynamo onset and when convective cells are localized close to the inner sphere. However, we know from hydrodynamic studies that the convection cells move towards the outer shell when the stratification is increased (Jones, Kuzanyan & Mitchell 2009; Gastine & Wicht 2012), which explains why this feature tends to disappear in Figs 1(d) and (f). Besides, we see in Fig. 4 that the values of $f_{\mathrm{dip}_{ax}}$ tend to decrease with N_ϱ, which is also clear if we focus for instance on the dipolar branch in Fig. 1(f) for which $f_{\mathrm{dip}_{ax}} < 0.8$. As expected, this indicates that the small magnetic scales at the outer surface are favoured with the increase of the stratification. This is also clearly confirmed by the comparison of the radial magnetic fields at the outer surface of the model, as shown in the left-hand panels of Figs 5 and 6. Finally, we also report the existence of multipolar dynamos whose dipolarity displays strong variations in time. This leads to averaged values of $f_{\mathrm{dip}_{ax}} \sim 0.5$, as one can notice in Fig. 1(d). These dynamos usually exhibit a relatively strong axial dipole component which undergoes reversals during which the value of $f_{\mathrm{dip}_{ax}}$ decreases drastically. Duarte et al. (2013) also reported similar behaviour for dynamo models with a variable electrical conductivity.

For $N_\varrho > 2.0$, we found that the dipole collapse tends to occur at values of Ro$_\ell$ lower than 0.1. However, it is likely that a volume-averaged quantity becomes less relevant when applied to models
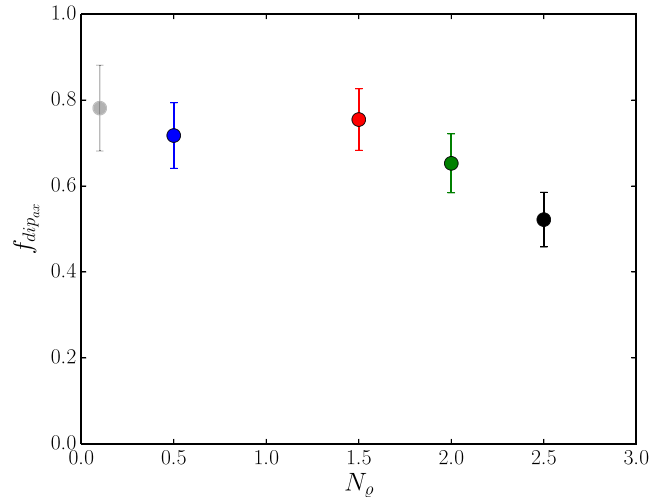
Figure 4. Average values of $f_{\mathrm{dip}_{ax}}$ for dipolar dynamos as a function of N_ϱ. Error bars represent the standard deviation. The average is done with 11 models for $N_\varrho = 2.5$.

with a substantial stratification. For instance, we see in Figs 5(b) and 6(b) that the smaller structures that develop at $N_\varrho = 2.5$ are confined close to the outer boundary, whereas there are no significant differences in the radial flow at mid-depth. Thus, we also examined the radial dependence of the different components of the local Rossby number Ro$_\ell^\star$, which is computed as the product of two terms: a convective Rossby number based on the velocity field $\boldsymbol{v}_c$ from which the mean zonal flow has been subtracted (see Fig. 7a) and a characteristic length-scale based on the mean harmonic degree of $\boldsymbol{v}_c$ (see Fig. 7b). We find that the monotonicity of Ro$_l^\star$ changes as N_ϱ is increased. Indeed, for low stratifications, Ro$_l^\star(r)$ mainly decreases with radius, whereas for $N_\varrho \geq 2.5$ it becomes an increasing function of r that steepens slightly close to the outer surface. Fig. 7(c) shows the evolution of Ro$_l^\star(r)$ for increasing Rayleigh numbers up to the loss of the dipolar solution, at $N_\varrho = 2.5$ and 3.0. When the transition to the multipolar branch is reached, we see that Ro$_\ell^\star$ tends to increase faster close to the outer surface, while the volume-averaged value can stay below the critical value of 0.1. Thus, it seems that inertia still causes the collapse of the dipolar branch, despite the fact that the usual local Rossby number criterion is not appropriate to separate the two dynamo branches for significant density stratifications.

3.4 Dynamo mechanisms

Finally, we try to investigate whether the dynamo mechanisms at work on the dipolar branch are modified when the stratification is increased. We see in Fig. 8 that the axisymmetric azimuthal magnetic field we observe at $N_\varrho = 1.5$ is strongly reminiscent of the magnetic structures that can be observed with Boussinesq models, which are usually interpreted in terms of α^2 dynamos (Olson, Christensen & Glatzmaier 1999; Schrinner et al. 2007, 2012; Schrinner, Petitdemange & Dormy 2011). Inside the tangent cylinder, the azimuthal magnetic field is mainly produced by the Ω-effect, $r \overline{B}_r \partial \left(r^{-1} \overline{V}_\varphi \right) / \partial r + r^{-1} \sin \theta \, \overline{B}_\theta \partial \left(\sin \theta^{-1} \overline{V}_\varphi \right) / \partial \theta$, which correlates inside the tangent cylinder with the axisymmetric azimuthal magnetic field, when comparing Figs 8(b) and (c). However, outside the tangent cylinder, the large part of the mean azimuthal field does not seem to be the result of the Ω-effect, and it is thus likely that the

---

[2] For instance, one can compare the models 008d, 055d and 083d for which Ra/Ra$_c \sim 6$ and an increasing Ro of 4.8×10^{-3}, 1.3×10^{-2} and 1.8×10^{-2}, respectively, or else the models 021d, 051d and 096d that have a similar Rossby number of 0.01, but for which Ra/Ra$_c$ is about 12, 5 and 2.9, respectively.

(a) $N_\varrho = 1.5$ (b) $N_\varrho = 1.5$
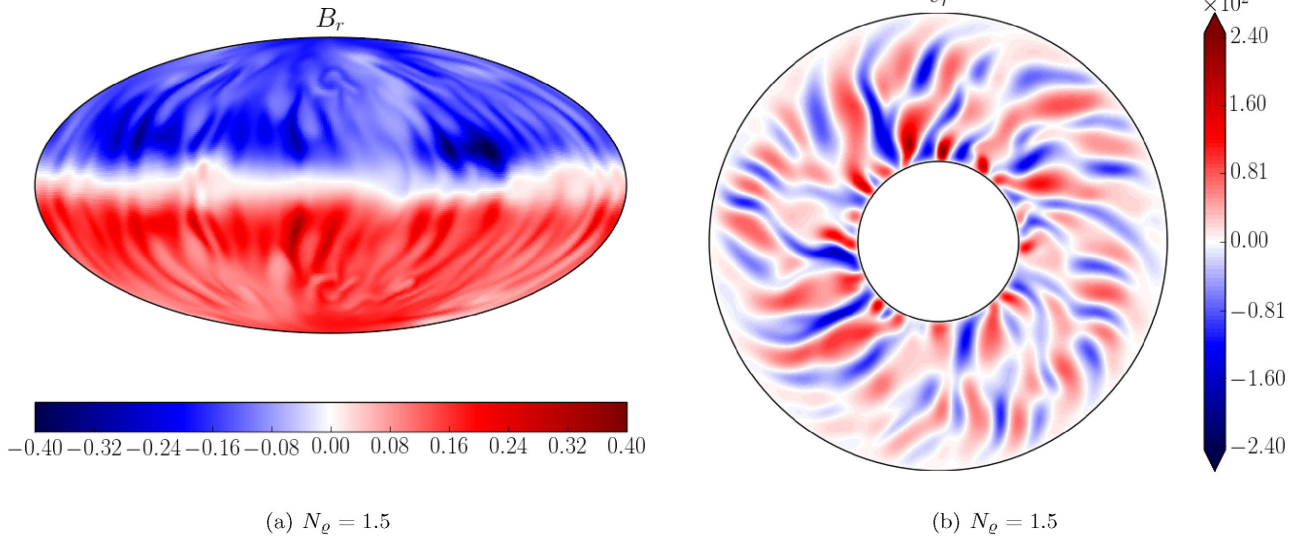
Figure 5. Snapshot of $B_r(r = r_o)$ (a) and equatorial cut of v_r (b) for a dipolar dynamo with $N_\varrho = 1.5$, $Pm = 0.75$, $Ra = 4.625 \times 10^6 = 5Ra_c$.

(a) $N_\varrho = 2.5$ (b) $N_\varrho = 2.5$
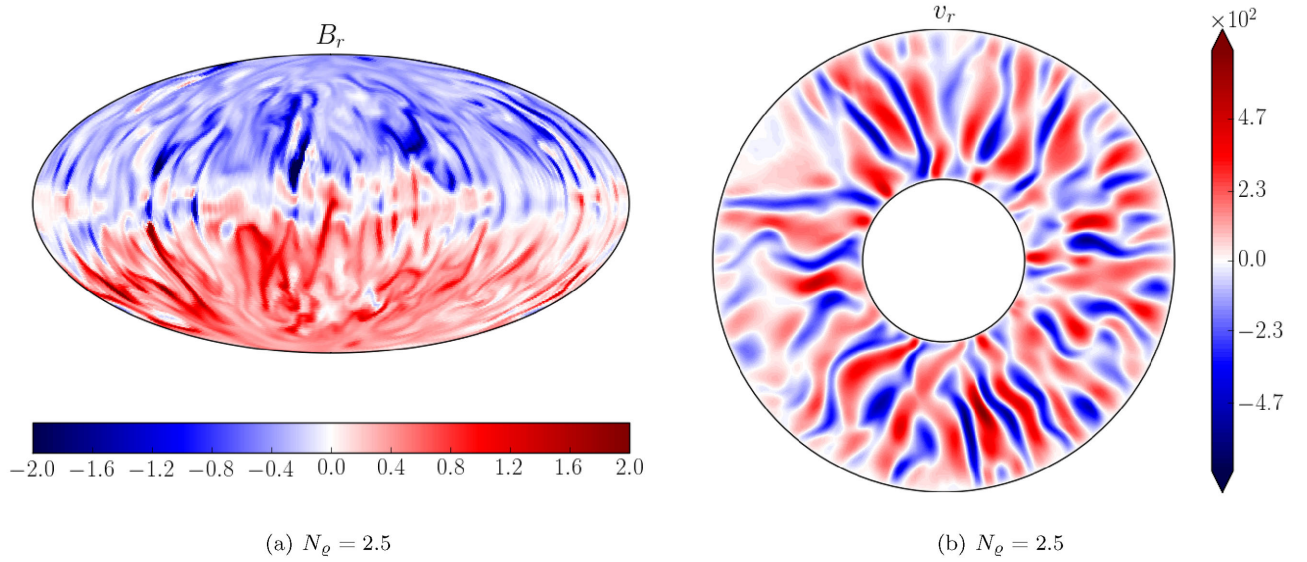
Figure 6. Snapshot of $B_r(r = r_o)$ (a) and equatorial cut of v_r (b) for a dipolar dynamo with $N_\varrho = 2.5$, $Pm = 2$, $Ra = 7.40 \times 10^6 = 3.4Ra_c$.
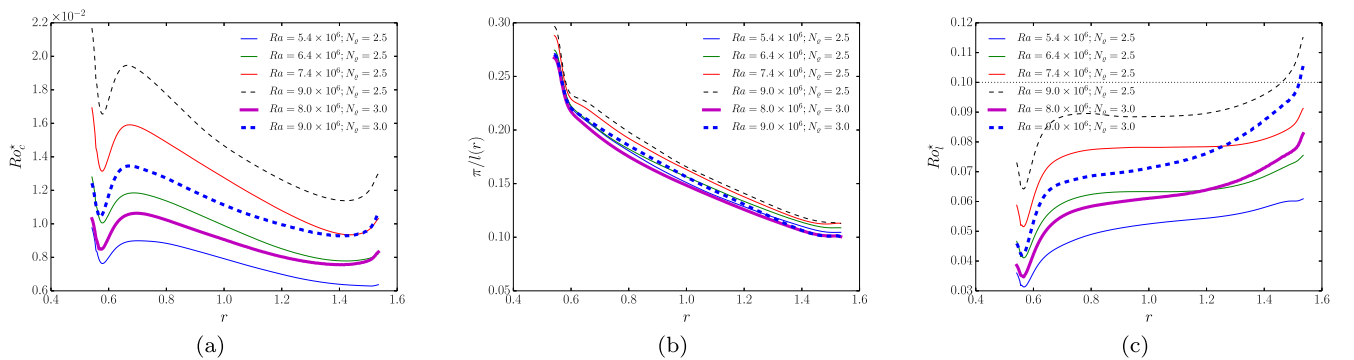
Figure 7. The convective Rossby number (a), the convective length-scale (b) and the local Rossby number (c) as a function of radius for dipolar (solid lines) and multipolar (dashed lines) dynamos at ($N_\varrho = 2.5$, $Pm = 2$) (thin lines) and ($N_\varrho = 3$, $Pm = 4$) (thick lines).

(a) $N_\varrho = 1.5$ (b) $N_\varrho = 1.5$ (c) $N_\varrho = 1.5$
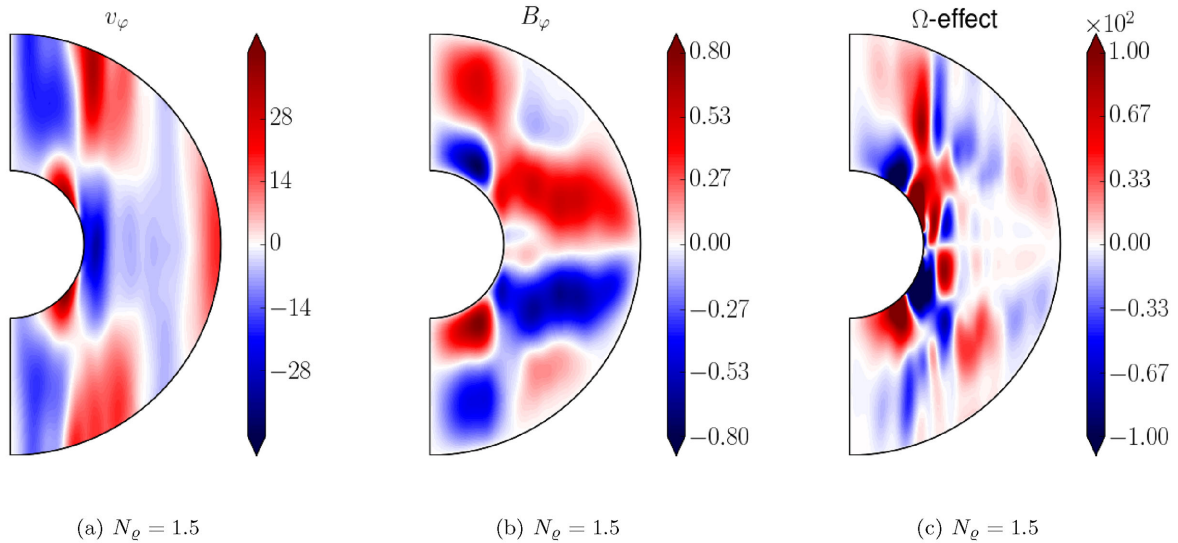
Figure 8. Time-averaged axisymmetric component of the azimuthal magnetic field (top) and velocity field (bottom) for a dipolar dynamo with $N_\varrho = 1.5$, Ra $= 4.625 \times 10^6$, Pm $= 0.75$.

(a) $N_\varrho = 2.5$ (b) $N_\varrho = 2.5$ (c) $N_\varrho = 2.5$
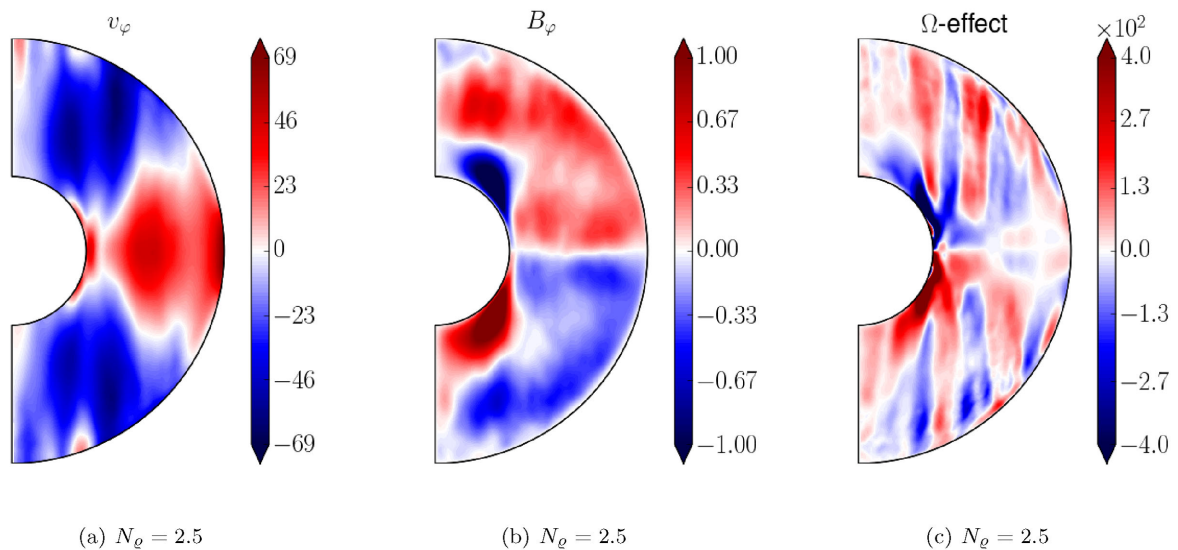
Figure 9. Time-averaged axisymmetric component of the azimuthal magnetic field (top) and velocity field (bottom) for a dipolar dynamo with $N_\varrho = 2.5$, Ra $= 7.40 \times 10^6$, Pm $= 2$.

essential regeneration of the poloidal field is achieved by α-effect, leading to the emergence of characteristic equatorial patches of opposite polarity (see e.g. Christensen 2011; Schrinner et al. 2012). We did not find in our sample of models tangible evidence that would invalidate this scenario at higher N_ϱ. For instance, at $N_\varrho = 2.5$, we see in Fig. 9 that the major differences lie in the stronger axisymmetric azimuthal velocity (compare Figs 8a and 9a). Nevertheless, the axisymmetric azimuthal magnetic field shown in Fig. 9(b) seems only modified about a colatitude $\theta \sim \pi/4$ close to the outer surface, and keeps now the same polarity in each hemisphere outside the tangent cylinder. This change can be correlated to the modifications of the axisymmetric azimuthal velocity, which in turn affect the Ω-effect (compare Figs 8c and 9c). Of course, we are for now limited to the observation of correlations, but it would be interesting to have a further insight into the dynamo mechanism in anelastic simulations

using a test field method, in the spirit of the Boussinesq study by Schrinner et al. (2012).

4 CONCLUSION

With this systematic parameter study, we are able to improve our understanding of the successive modifications that are exhibited by the stability domain of the dipolar branch when increasing the density stratification in anelastic dynamo models. In general, dipolar dynamos are found closer to the onset of convection. Moreover, we show that dipole-dominated solutions can be observed even at high-density stratifications, provided high enough magnetic Prandtl numbers are considered. Besides, this study also highlights why dipolar dynamos seem more difficult to find in anelastic simulations. Indeed, this tendency is usually reported as a general

statement, but here we show that this impression mainly results from the fact that the dipolar branch extends on a smaller and smaller range of Rayleigh numbers as N_ϱ is increased. However, despite the relative shrinking of the stability domain, we found that the critical magnetic Reynolds number of the dipolar branch seems scarcely modified in the overall process. At the same time, the higher N_ϱ, the faster convection will develop as we depart from the onset. In consequence, the higher N_ϱ, the faster is reached the critical Rossby number above which inertia causes the collapse of the dipole. This explains why dipolar dynamos become clearly confined in a smaller region of the parameter space. However, we stress that, in terms of magnetic Reynolds number, the dynamo threshold does not significantly increase with the density stratification in the range of N_ϱ we investigated.

In addition, this study also suggests that the scarcity of dipolar solutions for substantial density stratifications would thus rather come from the restriction of the parameter space being currently explored (because of computational limitations), rather than an intrinsic modification of the dynamo mechanisms that would be caused by the density stratification. Furthermore, if we decrease the Ekman number from $E = 10^{-4}$ to 3×10^{-5} keeping $Pr = 1$, we find that we recover three examples of bistable pairs at $N_\varrho = 2$, for $Pm = 1$ at $Ra/Ra_c = 2.6$ and for $Pm \in \{1, 2\}$ at $Ra/Ra_c = 2.9$. Then, beyond the results of this study, and for low values of the Ekman number that are currently very expensive to simulate, it seems more likely that dipolar solutions will persist in a larger region of parameter space (see also Duarte 2014; Jones 2014).

Despite the fact that it is not straightforward to relate the output of numerical models with observations (Gastine et al. 2013), the bistability that is reported for numerical simulations can be similarly observed with real objects. For instance, in a spectropolarimetric survey done with a sample of active M dwarfs, Morin et al. (2010) report two distinct categories of magnetic topologies. They distinguish strong axisymmetric dipolar fields and weak fields with significant non-axisymmetric components, and both configurations seem to be observed on objects with similar stellar parameters. After Schrinner et al. (2012), we show that the bistable behaviour observed in numerical models could be a possible way towards a better understanding of the broad diversity of the magnetic fields of M dwarfs, and that it cannot be ruled out even when taking into account the density stratification. The understanding of the impact of the stratification on the dynamo mechanisms deserves further studies.

ACKNOWLEDGEMENTS

REFERENCES

Alboussière T., Ricard Y., 2013, J. Fluid Mech., 725, 1
Anufriev A. P., Jones C. A., Soward A. M., 2005, Phys. Earth Planet. Inter., 152, 163
Berkoff N. A., Kersale E., Tobias S. M., 2010, Geophys. Astrophys. Fluid Dyn., 104, 545
Braginsky S. I., Roberts P. H., 1995, Geophys. Astrophys. Fluid Dyn., 79, 1
Brown B. P., Vasil G. M., Zweibel E. G., 2012, ApJ, 756, 109
Christensen U. R., 2011, Phys. Earth Planet. Inter., 187, 157
Christensen U. R., Aubert J., 2006, Geophys. J. Int., 166, 97
Donati J.-F., Landstreet J. D., 2009, ARA&A, 47, 333
Dormy E., Cardin P., Jault D., 1998, Earth Planet. Sci. Lett., 160, 15
Duarte L., 2014, PhD thesis, Technische Universität Braunschweig
Duarte L. D. V., Gastine T., Wicht J., 2013, Phys. Earth Planet. Inter., 222, 22
Gastine T., Wicht J., 2012, Icarus, 219, 428
Gastine T., Duarte L., Wicht J., 2012, A&A, 546, A19
Gastine T., Morin J., Duarte L., Reiners A., Christensen U. R., Wicht J., 2013, A&A, 549, L5
Gastine T., Wicht J., Duarte L. D. V., Heimpel M., Becker A., 2014, Geophys. Res. Lett., 41, 5410
Gilman P. A., Glatzmaier G. A., 1981, ApJS, 45, 335
Glatzmaier G. A., Roberts P. H., 1995, Nature, 377, 203
Gough D. O., 1969, J. Atmos. Sci., 26, 448
Jones C., 2014, Icarus, 241, 148
Jones C. A., Kuzanyan K. M., Mitchell R. H., 2009, J. Fluid Mech., 634, 291
Jones C. A., Boronski P., Brun A. S., Glatzmaier G. A., Gastine T., Miesch M. S., Wicht J., 2011, Icarus, 216, 120
Lantz S. R., Fan Y., 1999, ApJS, 121, 247
Larmor J., 1919, Report of the British Association for the Advancement of Science, 87th Meeting, p. 159, available at: https://archive.org/details/cbarchive_123167_howcouldarotatingbodysuchasthe1920
Morin J., Donati J.-F., Petit P., Delfosse X., Forveille T., Jardine M. M., 2010, MNRAS, 407, 2269
Ogura Y., Phillips N. A., 1962, J. Atmos. Sci., 19, 173
Olson P., Christensen U. R., Glatzmaier G. A., 1999, J. Geophys. Res., 104, 10383
Raynaud R., Petitdemange L., Dormy E., 2014, A&A, 567, A107
Sasaki Y., Takehiro S.-i., Kuramoto K., Hayashi Y.-Y., 2011, Phys. Earth Planet. Inter., 188, 203
Schrinner M., Rädler K.-H., Schmitt D., Rheinhardt M., Christensen U. R., 2007, Geophys. Astrophys. Fluid Dyn., 101, 81
Schrinner M., Petitdemange L., Dormy E., 2011, A&A, 530, A140
Schrinner M., Petitdemange L., Dormy E., 2012, ApJ, 752, 121
Schrinner M., Petitdemange L., Raynaud R., Dormy E., 2014, A&A, 564, A78
Yadav R. K., Gastine T., Christensen U. R., Duarte L. D. V., 2013, ApJ, 774, 6

APPENDIX A: NUMERICAL MODELS

Table A1. Overview of the simulations carried out, with $E = 10^{-4}$, $Pr = 1$, $\chi = 0.35$ and $n = 2$.

Model	N_ϱ	Ra	Pm	Ro	Ro_ℓ	Ro_z	Lo	$f_{dip_{ax}}$
001m	0.5	1.500×10^6	2.00	3.2×10^{-3}	2.0×10^{-2}	1.8×10^{-3}	2.3×10^{-3}	6.6×10^{-2}
002m	0.5	1.750×10^6	1.00	3.7×10^{-3}	2.2×10^{-2}	2.7×10^{-3}	1.8×10^{-3}	1.6×10^{-2}
003m	0.5	1.800×10^6	0.75	3.5×10^{-3}	2.8×10^{-2}	2.8×10^{-3}	1.9×10^{-3}	2.2×10^{-3}
004m	0.5	1.850×10^6	1.00	3.9×10^{-3}	2.4×10^{-2}	4.2×10^{-3}	2.0×10^{-3}	2.5×10^{-2}
005m	0.5	2.000×10^6	0.75	4.1×10^{-3}	2.3×10^{-2}	5.2×10^{-3}	2.4×10^{-3}	9.0×10^{-5}
006m	0.5	2.000×10^6	1.50	5.5×10^{-3}	2.8×10^{-2}	3.0×10^{-3}	3.1×10^{-3}	5.3×10^{-2}
007m	0.5	2.000×10^6	2.00	5.3×10^{-3}	2.7×10^{-2}	2.0×10^{-3}	3.7×10^{-3}	9.4×10^{-2}
008m	0.5	2.000×10^6	3.00	5.1×10^{-3}	2.7×10^{-2}	1.7×10^{-3}	4.1×10^{-3}	2.7×10^{-1}
008d	0.5	2.000×10^6	3.00	4.8×10^{-3}	2.6×10^{-2}	1.0×10^{-3}	5.5×10^{-3}	7.7×10^{-1}
009d	0.5	2.000×10^6	5.00	4.8×10^{-3}	2.5×10^{-2}	1.1×10^{-3}	5.7×10^{-3}	6.8×10^{-1}
010m	0.5	2.500×10^6	0.75	7.7×10^{-3}	3.3×10^{-2}	5.2×10^{-3}	3.8×10^{-3}	5.1×10^{-2}
011m	0.5	2.500×10^6	1.00	7.2×10^{-3}	3.5×10^{-2}	3.6×10^{-3}	4.5×10^{-3}	7.6×10^{-2}
012m	0.5	2.500×10^6	1.50	7.1×10^{-3}	3.5×10^{-2}	3.1×10^{-3}	4.5×10^{-3}	3.3×10^{-1}
013d	0.5	2.500×10^6	4.00	6.0×10^{-3}	3.3×10^{-2}	1.5×10^{-3}	6.9×10^{-3}	7.3×10^{-1}
014m	0.5	3.000×10^6	1.00	8.6×10^{-3}	4.2×10^{-2}	4.0×10^{-3}	5.5×10^{-3}	1.3×10^{-1}
015m	0.5	3.000×10^6	2.00	8.2×10^{-3}	4.2×10^{-2}	2.8×10^{-3}	6.3×10^{-3}	3.0×10^{-1}
015d	0.5	3.000×10^6	2.00	7.5×10^{-3}	3.9×10^{-2}	1.7×10^{-3}	7.9×10^{-3}	7.5×10^{-1}
016d	0.5	3.000×10^6	3.00	7.5×10^{-3}	4.0×10^{-2}	1.7×10^{-3}	8.5×10^{-3}	7.2×10^{-1}
017d	0.5	3.000×10^6	4.00	7.5×10^{-3}	4.0×10^{-2}	1.7×10^{-3}	8.5×10^{-3}	7.2×10^{-1}
018d	0.5	3.000×10^6	5.00	7.5×10^{-3}	4.1×10^{-2}	1.8×10^{-3}	8.8×10^{-3}	6.8×10^{-1}
019d	0.5	3.000×10^6	6.00	7.6×10^{-3}	4.1×10^{-2}	1.9×10^{-3}	9.0×10^{-3}	6.4×10^{-1}
020m	0.5	4.000×10^6	0.50	1.3×10^{-2}	5.3×10^{-2}	9.3×10^{-3}	6.6×10^{-3}	2.3×10^{-1}
021m	0.5	4.000×10^6	1.00	1.2×10^{-2}	5.6×10^{-2}	5.7×10^{-3}	7.9×10^{-3}	2.8×10^{-1}
021d	0.5	4.000×10^6	1.00	1.0×10^{-2}	5.4×10^{-2}	2.0×10^{-3}	1.1×10^{-2}	8.7×10^{-1}
022m	0.5	4.000×10^6	2.00	1.5×10^{-2}	5.7×10^{-2}	3.5×10^{-3}	8.8×10^{-3}	2.6×10^{-1}
022d	0.5	4.000×10^6	2.00	1.0×10^{-2}	5.4×10^{-2}	1.9×10^{-3}	1.1×10^{-2}	6.6×10^{-1}
023d	0.5	4.000×10^6	3.00	1.0×10^{-2}	5.3×10^{-2}	2.0×10^{-3}	1.1×10^{-2}	6.8×10^{-1}
024d	0.5	4.000×10^6	4.00	1.0×10^{-2}	5.3×10^{-2}	1.9×10^{-3}	1.1×10^{-2}	6.5×10^{-1}
025d	0.5	4.000×10^6	6.00	1.0×10^{-2}	5.3×10^{-2}	2.2×10^{-3}	1.2×10^{-2}	5.4×10^{-1}
026m	0.5	5.000×10^6	0.50	1.5×10^{-2}	6.8×10^{-2}	8.4×10^{-3}	8.8×10^{-3}	2.3×10^{-1}
027m	0.5	5.000×10^6	1.00	1.4×10^{-2}	7.1×10^{-2}	5.5×10^{-3}	1.0×10^{-2}	2.5×10^{-1}
027d	0.5	5.000×10^6	1.00	1.3×10^{-2}	6.7×10^{-2}	2.0×10^{-3}	1.4×10^{-2}	8.1×10^{-1}
028d	0.5	5.000×10^6	2.00	1.3×10^{-2}	6.6×10^{-2}	2.2×10^{-3}	1.4×10^{-2}	6.8×10^{-1}
029d	0.5	5.000×10^6	3.00	1.3×10^{-2}	6.8×10^{-2}	2.1×10^{-3}	1.4×10^{-2}	7.2×10^{-1}
030d	0.5	5.000×10^6	4.00	1.3×10^{-2}	6.5×10^{-2}	2.5×10^{-3}	1.6×10^{-2}	7.0×10^{-1}
031d	0.5	5.000×10^6	5.00	1.3×10^{-2}	6.7×10^{-2}	2.5×10^{-3}	1.5×10^{-2}	6.8×10^{-1}
032m	0.5	6.000×10^6	1.00	1.7×10^{-2}	8.5×10^{-2}	6.3×10^{-3}	1.3×10^{-2}	2.8×10^{-1}
032d	0.5	6.000×10^6	1.00	1.5×10^{-2}	8.0×10^{-2}	2.6×10^{-3}	1.7×10^{-2}	8.2×10^{-1}
033m	0.5	7.000×10^6	1.00	2.0×10^{-2}	9.6×10^{-2}	7.4×10^{-3}	1.4×10^{-2}	2.5×10^{-1}
033d	0.5	7.000×10^6	1.00	1.8×10^{-2}	8.6×10^{-2}	3.0×10^{-3}	2.0×10^{-2}	8.5×10^{-1}
034m	0.5	9.000×10^6	1.00	2.5×10^{-2}	1.2×10^{-1}	8.2×10^{-3}	1.9×10^{-2}	3.6×10^{-1}
035m	0.5	1.000×10^7	1.00	2.7×10^{-2}	1.3×10^{-1}	8.7×10^{-3}	2.1×10^{-2}	3.4×10^{-1}
036m	1.5	2.500×10^6	0.75	3.9×10^{-3}	2.6×10^{-2}	2.9×10^{-3}	3.3×10^{-3}	4.7×10^{-2}
037m	1.5	2.500×10^6	1.00	4.5×10^{-3}	2.7×10^{-2}	2.0×10^{-3}	3.6×10^{-3}	1.9×10^{-1}
038m	1.5	2.500×10^6	1.50	4.3×10^{-3}	2.8×10^{-2}	9.2×10^{-4}	4.4×10^{-3}	1.0×10^{-1}
038d	1.5	2.500×10^6	1.50	4.3×10^{-3}	2.8×10^{-2}	8.2×10^{-4}	5.0×10^{-3}	7.9×10^{-1}
039d	1.5	2.500×10^6	2.00	4.3×10^{-3}	3.0×10^{-2}	7.7×10^{-4}	4.6×10^{-3}	7.1×10^{-1}
040d	1.5	2.500×10^6	3.00	4.2×10^{-3}	2.9×10^{-2}	8.0×10^{-4}	4.8×10^{-3}	7.3×10^{-1}
041m	1.5	3.000×10^6	0.75	5.5×10^{-3}	3.6×10^{-2}	2.9×10^{-3}	4.8×10^{-3}	2.1×10^{-1}
042m	1.5	3.000×10^6	1.00	6.0×10^{-3}	3.6×10^{-2}	2.0×10^{-3}	5.1×10^{-3}	3.9×10^{-1}
042d	1.5	3.000×10^6	1.00	5.7×10^{-3}	3.7×10^{-2}	1.1×10^{-3}	6.4×10^{-3}	8.5×10^{-1}
043d	1.5	3.000×10^6	2.00	5.5×10^{-3}	3.7×10^{-2}	1.1×10^{-3}	6.2×10^{-3}	7.1×10^{-1}
044d	1.5	3.700×10^6	3.00	7.3×10^{-3}	4.7×10^{-2}	1.4×10^{-3}	7.9×10^{-3}	6.0×10^{-1}
045m	1.5	4.000×10^6	0.50	9.5×10^{-3}	4.9×10^{-2}	5.3×10^{-3}	6.2×10^{-3}	2.8×10^{-1}
046m	1.5	4.000×10^6	0.75	8.7×10^{-3}	5.2×10^{-2}	3.0×10^{-3}	6.9×10^{-3}	4.5×10^{-1}
046d	1.5	4.000×10^6	0.75	8.5×10^{-3}	5.3×10^{-2}	1.5×10^{-3}	9.3×10^{-3}	8.2×10^{-1}
047d	1.5	4.000×10^6	1.00	8.5×10^{-3}	5.2×10^{-2}	1.4×10^{-3}	9.4×10^{-3}	7.8×10^{-1}
048d	1.5	4.000×10^6	2.00	8.5×10^{-3}	5.3×10^{-2}	1.5×10^{-3}	8.4×10^{-3}	6.9×10^{-1}
049m	1.5	4.625×10^6	0.50	9.5×10^{-3}	5.8×10^{-2}	6.0×10^{-3}	7.5×10^{-3}	4.5×10^{-1}
050m	1.5	4.625×10^6	0.75	1.0×10^{-2}	6.2×10^{-2}	3.6×10^{-3}	8.1×10^{-3}	5.3×10^{-1}

Table A1. – *continued.*

Model	N_ϱ	Ra	Pm	Ro	Ro_ℓ	Ro_z	Lo	$f_{\mathrm{dip}_{\mathrm{ax}}}$
050d	1.5	4.625×10^6	0.75	1.0×10^{-2}	6.2×10^{-2}	1.7×10^{-3}	1.1×10^{-2}	8.6×10^{-1}
051d	1.5	4.625×10^6	1.00	1.0×10^{-2}	6.3×10^{-2}	1.7×10^{-3}	1.1×10^{-2}	7.6×10^{-1}
052d	1.5	5.000×10^6	1.00	1.1×10^{-2}	6.7×10^{-2}	1.8×10^{-3}	1.2×10^{-2}	7.5×10^{-1}
053d	1.5	5.000×10^6	2.00	1.1×10^{-2}	6.7×10^{-2}	1.8×10^{-3}	1.2×10^{-2}	6.5×10^{-1}
054m	1.5	5.550×10^6	0.75	1.2×10^{-2}	7.4×10^{-2}	4.0×10^{-3}	9.9×10^{-3}	4.7×10^{-1}
054d	1.5	5.550×10^6	0.75	1.3×10^{-2}	7.7×10^{-2}	2.0×10^{-3}	1.4×10^{-2}	8.4×10^{-1}
055d	1.5	5.550×10^6	1.00	1.3×10^{-2}	7.7×10^{-2}	2.1×10^{-3}	1.3×10^{-2}	7.4×10^{-1}
056d	1.5	5.550×10^6	2.00	1.2×10^{-2}	7.4×10^{-2}	–	1.5×10^{-2}	6.3×10^{-1}
057m	1.5	6.500×10^6	0.50	1.6×10^{-2}	8.8×10^{-2}	5.5×10^{-3}	1.1×10^{-2}	4.1×10^{-1}
058m	1.5	6.500×10^6	0.75	1.5×10^{-2}	8.8×10^{-2}	4.3×10^{-3}	1.2×10^{-2}	4.8×10^{-1}
058d	1.5	6.500×10^6	0.75	1.5×10^{-2}	8.9×10^{-2}	2.4×10^{-3}	1.6×10^{-2}	8.3×10^{-1}
059d	1.5	6.500×10^6	1.00	1.5×10^{-2}	8.8×10^{-2}	2.5×10^{-3}	1.6×10^{-2}	7.7×10^{-1}
060m	1.5	8.000×10^6	0.75	1.9×10^{-2}	1.1×10^{-1}	5.4×10^{-3}	1.5×10^{-2}	3.8×10^{-1}
060d	1.5	8.000×10^6	0.75	1.9×10^{-2}	1.1×10^{-1}	3.3×10^{-3}	2.0×10^{-2}	8.2×10^{-1}
061d	1.5	8.000×10^6	1.00	1.9×10^{-2}	1.1×10^{-1}	3.0×10^{-3}	2.0×10^{-2}	7.7×10^{-1}
062m	1.5	9.000×10^6	0.50	2.2×10^{-2}	1.2×10^{-1}	6.4×10^{-3}	1.6×10^{-2}	4.5×10^{-1}
063m	1.5	9.000×10^6	1.00	2.2×10^{-2}	1.2×10^{-1}	5.1×10^{-3}	1.8×10^{-2}	3.1×10^{-1}
064m	1.5	1.000×10^7	0.50	2.5×10^{-2}	1.3×10^{-1}	8.0×10^{-3}	1.8×10^{-2}	3.0×10^{-1}
065m	2.0	3.000×10^6	1.00	4.0×10^{-3}	2.9×10^{-2}	1.8×10^{-3}	3.8×10^{-3}	2.2×10^{-1}
066d	2.0	3.000×10^6	2.00	4.0×10^{-3}	3.1×10^{-2}	5.5×10^{-4}	4.5×10^{-3}	7.7×10^{-1}
067m	2.0	4.000×10^6	1.00	6.8×10^{-3}	4.6×10^{-2}	1.7×10^{-3}	6.0×10^{-3}	2.9×10^{-1}
068d	2.0	4.000×10^6	2.00	6.5×10^{-3}	4.6×10^{-2}	1.1×10^{-3}	7.2×10^{-3}	7.2×10^{-1}
069d	2.0	4.000×10^6	3.00	6.6×10^{-3}	4.6×10^{-2}	1.1×10^{-3}	7.3×10^{-3}	6.4×10^{-1}
070m	2.0	5.000×10^6	0.50	8.3×10^{-3}	5.5×10^{-2}	5.4×10^{-3}	6.4×10^{-3}	2.3×10^{-1}
071m	2.0	5.000×10^6	1.00	9.2×10^{-3}	6.0×10^{-2}	2.1×10^{-3}	7.5×10^{-3}	2.9×10^{-1}
072d	2.0	5.000×10^6	1.50	9.3×10^{-3}	6.4×10^{-2}	1.6×10^{-3}	9.9×10^{-3}	6.8×10^{-1}
073d	2.0	5.000×10^6	2.00	9.1×10^{-3}	6.4×10^{-2}	1.7×10^{-3}	1.0×10^{-2}	6.3×10^{-1}
074d	2.0	5.000×10^6	3.00	9.0×10^{-3}	6.1×10^{-2}	1.5×10^{-3}	1.0×10^{-2}	6.1×10^{-1}
075m	2.0	6.000×10^6	0.50	1.1×10^{-2}	7.3×10^{-2}	4.1×10^{-3}	8.2×10^{-3}	2.5×10^{-1}
076d	2.0	6.000×10^6	2.00	1.2×10^{-2}	7.9×10^{-2}	2.0×10^{-3}	1.3×10^{-2}	5.6×10^{-1}
077m	2.0	7.000×10^6	0.70	1.5×10^{-2}	8.7×10^{-2}	4.0×10^{-3}	1.2×10^{-2}	1.7×10^{-1}
078m	2.0	7.000×10^6	1.00	1.4×10^{-2}	9.0×10^{-2}	3.0×10^{-3}	1.2×10^{-2}	4.4×10^{-1}
079d	2.0	7.000×10^6	1.50	1.4×10^{-2}	9.0×10^{-2}	1.9×10^{-3}	1.6×10^{-2}	5.9×10^{-1}
080d	2.0	7.000×10^6	2.00	1.4×10^{-2}	8.8×10^{-2}	1.7×10^{-3}	1.6×10^{-2}	6.7×10^{-1}
081d	2.0	7.000×10^6	3.00	1.4×10^{-2}	9.1×10^{-2}	1.9×10^{-3}	1.7×10^{-2}	5.7×10^{-1}
082m	2.0	8.500×10^6	0.50	1.8×10^{-2}	1.1×10^{-1}	4.6×10^{-3}	1.3×10^{-2}	3.9×10^{-1}
083d	2.0	8.500×10^6	2.00	1.8×10^{-2}	1.1×10^{-1}	2.9×10^{-3}	1.9×10^{-2}	7.5×10^{-1}
084m	2.0	1.000×10^7	0.50	2.2×10^{-2}	1.2×10^{-1}	7.3×10^{-3}	1.6×10^{-2}	2.7×10^{-1}
085m	2.0	1.000×10^7	3.00	2.0×10^{-2}	1.2×10^{-1}	3.9×10^{-3}	2.1×10^{-2}	2.1×10^{-1}
086m	2.0	1.200×10^7	0.50	2.6×10^{-2}	1.4×10^{-1}	8.0×10^{-3}	1.8×10^{-2}	3.9×10^{-1}
087m	2.0	1.400×10^7	0.50	3.0×10^{-2}	1.6×10^{-1}	1.0×10^{-2}	2.1×10^{-2}	3.9×10^{-1}
088d	2.5	3.200×10^6	4.00	2.6×10^{-3}	2.0×10^{-2}	3.2×10^{-4}	3.6×10^{-3}	5.2×10^{-1}
089d	2.5	3.400×10^6	4.00	3.1×10^{-3}	2.4×10^{-2}	3.7×10^{-4}	3.8×10^{-3}	6.0×10^{-1}
090d	2.5	4.400×10^6	3.00	5.7×10^{-3}	4.5×10^{-2}	8.1×10^{-4}	7.0×10^{-3}	5.5×10^{-1}
091d	2.5	4.400×10^6	4.00	5.4×10^{-3}	4.1×10^{-2}	7.5×10^{-4}	6.8×10^{-3}	5.2×10^{-1}
092d	2.5	5.400×10^6	2.00	8.0×10^{-3}	5.9×10^{-2}	1.1×10^{-3}	9.3×10^{-3}	4.0×10^{-1}
093d	2.5	5.400×10^6	3.00	7.9×10^{-3}	5.9×10^{-2}	1.1×10^{-3}	1.0×10^{-2}	5.6×10^{-1}
094d	2.5	5.400×10^6	4.00	7.6×10^{-3}	5.6×10^{-2}	1.1×10^{-3}	1.1×10^{-2}	5.0×10^{-1}
095m	2.5	6.400×10^6	1.00	9.8×10^{-3}	7.2×10^{-2}	2.0×10^{-3}	9.0×10^{-3}	1.3×10^{-1}
096d	2.5	6.400×10^6	2.00	1.0×10^{-2}	7.1×10^{-2}	1.2×10^{-3}	1.2×10^{-2}	4.3×10^{-1}
097d	2.5	6.400×10^6	3.00	9.7×10^{-3}	6.9×10^{-2}	1.3×10^{-3}	1.4×10^{-2}	5.5×10^{-1}
098m	2.5	7.400×10^6	1.00	1.2×10^{-2}	8.3×10^{-2}	2.4×10^{-3}	1.1×10^{-2}	1.5×10^{-1}
099d	2.5	7.400×10^6	2.00	1.3×10^{-2}	8.4×10^{-2}	1.8×10^{-3}	1.5×10^{-2}	6.3×10^{-1}
100d	2.5	7.400×10^6	3.00	1.2×10^{-2}	8.4×10^{-2}	1.9×10^{-3}	1.4×10^{-2}	4.8×10^{-1}
101m	2.5	9.000×10^6	2.00	1.5×10^{-2}	9.9×10^{-2}	3.6×10^{-3}	1.5×10^{-2}	1.5×10^{-1}
102m	2.5	1.000×10^7	1.00	1.8×10^{-2}	1.3×10^{-1}	4.8×10^{-3}	1.4×10^{-2}	1.2×10^{-1}
103m	2.5	1.100×10^7	1.00	2.4×10^{-2}	1.5×10^{-1}	5.8×10^{-3}	1.6×10^{-2}	1.0×10^{-1}
104d	3.0	8.000×10^6	4.00	9.2×10^{-3}	6.9×10^{-2}	1.4×10^{-3}	1.4×10^{-2}	6.0×10^{-1}
105m	3.0	9.000×10^6	4.00	1.2×10^{-2}	8.6×10^{-2}	3.0×10^{-3}	1.4×10^{-2}	3.2×10^{-1}

This paper has been typeset from a TEX/LATEX file prepared by the author.